SCIENCE CHINA
Information Sciences

• RESEARCH PAPER •

May 2024, Vol. 67, Iss. 5, 152404:1–152404:9
https://doi.org/10.1007/s11432-023-3941-4

Layer-by-layer epitaxy growth of thickness-controllable two-dimensional tungsten disulfide

Jieyuan LIANG[1†], Zixing ZOU[3†], Junwu LIANG[4†], Di WANG[5], Biao WANG[1], Anshi CHU[1], Jiali YI[1], Cheng ZHANG[1], Lizhen FANG[1], Tian ZHANG[1], Huawei LIU[1], Xiaoli ZHU[1*], Dong LI[1*] & Anlian PAN[1,2*]

[1]*Key Laboratory for Micro-Nano Physics and Technology of Hunan Province, State Key Laboratory of Chemo/Biosensing and Chemometrics, Hunan Institute of Optoelectronic Integration, College of Materials Science and Engineering, School of Physics and Electronics, Hunan University, Changsha* 410082*, China;*
[2]*School of Physics and Electronics, Hunan Normal University, Changsha* 410081*, China;*
[3]*School of Electronic Information and Electrical Engineering, Changsha University, Changsha* 410022*, China;*
[4]*School of Physics and Telecommunication Engineering, Yulin Normal University, Yulin* 537000*, China;*
[5]*Units Semiconductor Technology Co., Ltd., Nanjing* 210000*, China*

Received 16 September 2023/Revised 26 October 2023/Accepted 18 January 2024/Published online 23 April 2024

Abstract Bilayer transition metal dichalcogenides (TMDs) balance the high mobility of single layers with the high state density of multilayers and therefore have promising application prospects in high-performance electronics. However, the layer-controlled growth of 2D materials is still confronted with challenges such as poor repeatability between different labs and a limited understanding of the growth mechanism at the atomic scale. Herein, we report a new carbon-assisted chemical vapor deposition process that can realize the growth of WS_2 sheets with high yield, precise thickness controllability, and repeatability. We show that carbon can act as a reducing agent and catalyst that preferentially reacts with the WO_3 precursor to form intermediate WO_{3-x} products with low-valence state W. The resulting oxycarbide gas has a low surface adsorption energy when deposited on the surface of as-grown WS_2, which provides nucleation sites for the subsequent layer of WS_2 growth and leads to the vertical growth of WS_2 sheets. The growth mechanism is thoroughly investigated. Electrical transport measurements show that the produced bilayer WS_2 possesses a high carrier mobility (up to 58 $cm^2 \cdot V^{-1} \cdot s^{-1}$) and small subthreshold swing (estimated to be 148 mV/decade), which are among the best reported results for TMDs produced using CVD.

Keywords WS_2, thickness-controlled growth, chemical vapor deposition, additive, carbon

1 Introduction

As Moore's law reaches its scaling limits, the search for new materials with superior properties in the post-silicon era has become a topic of great interest [1–4]. Two-dimensional transition metal dichalcogenides (2D TMDs) are prime candidates for satisfying the requirements of advanced technology beyond silicon because they are ultrathin and offer dangling bond-free surfaces, excellent electrostatic control, high theoretical mobility, and tunable band gaps [5–7]. One of the most intriguing properties of 2D TMDs is the correlation between their physical and chemical properties and the number of layers, which allows their electrical, optical, and optoelectronic properties to be welltuned through thickness modulation [8–10]. For example, the typical transition from an indirect to direct band gap that occurs as the thickness of a 2D TMD decreases to that of a monolayer has great potential in photonics [11]. For electrical applications, the three-atom thickness of monolayer TMDs causes them to be fragile and prone to damage during high-energy metal deposition processes, which leads to Femi level pinning and limits the performance of

* Corresponding author (email: zhuxiaoli@hnu.edu.cn, liidong@hnu.edu.cn, anlian.pan@hnu.edu.cn)
† Liang J Y, Zou Z X, and Liang J W have the same contribution to this work.

© Science China Press 2024

monolayer TMD-based electronic devices [12]. In comparison, the higher robustness of bilayer or trilayer TMDs during the device manufacturing process is advantageous in electronics because of the resultant lower Schottky barrier heights and contact resistance [13–15]. It is therefore crucial to engineer the thickness of 2D materials, especially in a well-controlled manner.

Significant progress has been achieved in the preparation of monolayer TMDs using chemical vapor deposition (CVD) [16]. However, the fabrication of bilayer or multilayer TMDs using CVD remains challenging. Although the CVD growth of monolayer TMDs is sometimes accompanied by the appearance of bilayer or multilayer TMDs, the effective application of these multilayers is hindered by their uncontrollability. Significant efforts are currently being made to control the thickness of TMDs epitaxially. For example, Wang et al [17] reported the growth of bilayer MoS_2 by inducing stepwise formation on a sapphire substrate. Uniform bilayer nucleation can be induced along the edge of a c-plane sapphire surface with an engineered atomic terrace height of 1.48 nm for the continuous epitaxy growth of bilayer crystal films. This technique is more suitable for sapphire substrates, which have ordered crystal structures and orientations, than for amorphous SiO_2/Si substrates that are compatible with the device fabrication process. In addition, only limited success has been achieved in controlling the layer number for the preparation of monolayer and bilayer TMD crystals via atomic terrace height modification on sapphire surfaces. In comparison, bottom-up layer-by-layer growth may provide a more feasible means for regulating thickness [18]. However, it faces the challenge that the nucleation and growth of an upper layer on top of a lower layer is extremely difficult because of the dangling bond-free surface and limited surface catalysts. It is essential that new and effective synthesis strategies to achieve nucleation on TMD surfaces be explored and the growth process and mechanisms of TMDs elucidated to achieve thickness-controlled growth.

In this study, we developed a carbon-assisted CVD method and successfully achieved the layer-by-layer growth of WS_2 crystals with high controllability, repeatability, and quality. Our results indicate that carbon promoted the production of low-valence tungsten oxide at high temperatures. The resulting oxycarbide by-products, which were preferentially deposited on the surface of the obtained WS_2 surface, provided nucleation sites for subsequent WS_2 layer growth. The high W/S ratio due to the additives also contributed to bilayer WS_2 growth and high-quality WS_2 flakes with tunable thicknesses. The as-grown bilayer WS_2 samples, which exhibit uniform and clean surfaces and single stacking directions, were systematically studied. A series of advanced characterization tools comprising optical microscopy, Raman spectroscopy, photoluminescence (PL), transmission electron microscopy (TEM), atomic force microscopy (AFM), and electrical transport measurements were used to evaluate the quality of the as-grown WS_2 bilayer samples. The results indicate high crystal quality in the samples, which could be used to construct transistors with high mobility (58 $cm^2 \cdot V^{-1} \cdot s^{-1}$) and low subthreshold swing (148 mV/decade).

2 Results and discussion

Bilayer WS_2 crystals were grown using carbon-assisted CVD, as shown in Figure 1(a). A precursor mixture comprising tungsten trioxide, carbon, and NaCl was ground thoroughly, mixed, and placed in a porcelain boat. Further details on the sample synthesis are provided in Section 4. Figures 1(b) and (c) show the microscopy images of the samples on SiO_2/Si substrates obtained with and without carbon in the precursor, respectively. Monolayer WS_2 triangular sheets were obtained without carbon (Figure 1(b)). In contrast, the addition of carbon in the precursor resulted in bilayer WS_2 triangular sheets (Figure 1(c)) with high density and perfectly equilateral triangular shapes, as shown in the low-magnification image (Figure S1). This indicates that excellent uniformity and high quality were achieved. High-resolution cross-sectional TEM was performed to determine the layer numbers of the WS_2 sheets obtained under different growth conditions. Figure 1(d) shows that the WS_2 obtained without carbon assistance has a monolayer nature with a layer thickness of approximately 0.65 nm whereas the WS_2 obtained with carbon assistance has two layers with a total thickness of 1.3 nm. The clean and sharp interfaces between the adjacent layers indicate superior epitaxy [19].

Figure 1(f) shows a summary of the average percentages of monolayer and bilayer WS_2 obtained with and without carbon in the precursor (50 samples for each group). It can be clearly seen that carbon played a crucial role in the growth of bilayer WS_2. The average percentage of monolayer WS_2 is 93% without carbon. The addition of carbon increased the average percentage of bilayer WS_2 to 95%, which surpasses that of monolayer WS_2. The as-grown monolayer and bilayer WS_2 crystals were further characterized

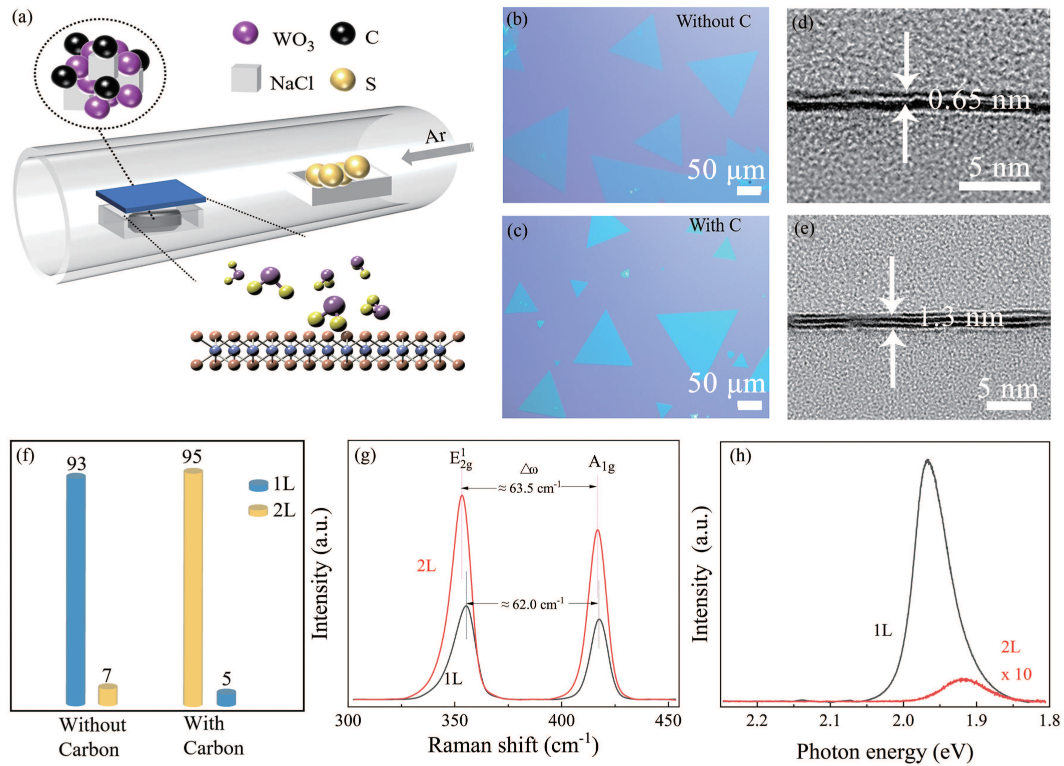

Figure 1 (Color online) Growth of bilayer WS_2. (a) Schematic illustration of bilayer WS_2 growth. Optical images of (b) monolayer WS_2 sheets obtained without the assistance of carbon and (c) bilayer WS_2 sheets obtained with the assistance of carbon. Cross-section TEM images of (d) monolayer and (e) bilayer WS_2. (f) Statistical percentages of monolayer and bilayer grown with and without the assistance of carbon. (g) Raman and (h) PL spectra of as-grown mono- and bilayer WS_2 crystals.

through Raman and photo-luminescence (PL) measurements and the results are presented in Figure 1(e). The E^1_{2g} and A_{1g} Raman modes were observed at 353.3 and 416.8 cm^{-1} in bilayer WS_2, respectively, and shifted to 355.4 and 417.4 cm^{-1} when the thickness was reduced to a monolayer. The peak frequency difference between the E^1_{2g} and A_{1g} modes reflects the number of layers in the WS_2 flakes because the difference decreases monotonically as the WS_2 thickness decreases. Accordingly, the frequency differences between the E^1_{2g} and A_{1g} modes in as-grown monolayer and bilayer WS_2 were estimated to be 62.0 and 63.5 cm^{-1}, respectively, which are in good agreement with those in previous reports [20]. Figure 1(h) shows the measured PL characteristics. The bilayer WS_2 sample produced a much weaker (100 times) PL signal compared to that of the monolayer WS_2 sample. This difference can be attributed to the transition from a direct band gap (monolayer) to an indirect one (bilayer). Additionally, the positions of the PL emission peaks were separately measured to be 1.97 eV (monolayer) and 1.92 eV (bilayer), which is consistent with previous reports [21].

The growth behavior of bilayer WS_2 was thoroughly investigated. As shown in Figures 2(a) and (b), layer-by-layer growth could be observed with the progress of growth time. The distinct optical contrast clearly reveals the morphological transformation of the bilayer WS_2 grains from incomplete to complete stacking under the assistance of carbon as the growth time increased from 2 to 5 min. The corresponding local AFM images clearly reveal the ultraclean and uniform surfaces of the obtained WS_2 crystals without deposited impurities on the surfaces. The continuous height steps from the substrate surface to the bottom monolayer and then to the upper monolayer shown in the height analysis results in the inset confirm the layer-by-layer stacking growth characteristics. The thickness of the upper layer is approximately 0.8 nm. The thickness of the bottom layer is nearly 1 nm larger than that of the monolayer because of the van der Waals gap between WS_2 and the substrate. The steps across the layers demonstrate that layer-by-layer growth dominated the growth of WS_2. Furthermore, as the growth time extended to longer durations (8–60 mins), trilayers, tetralayers, quintlayers, and even thicker WS_2 sheets were obtained (Figure 2(b)). The thicker films obtained after a growth time of 60 min can be attributed to the etching process due to local changes in the metal/chalcogenide ratio [22]. At longer growth times, the gradual consumption of W and sulfur improved the oxygen concentration, which led to the etching of the as-grown thin WS_2.

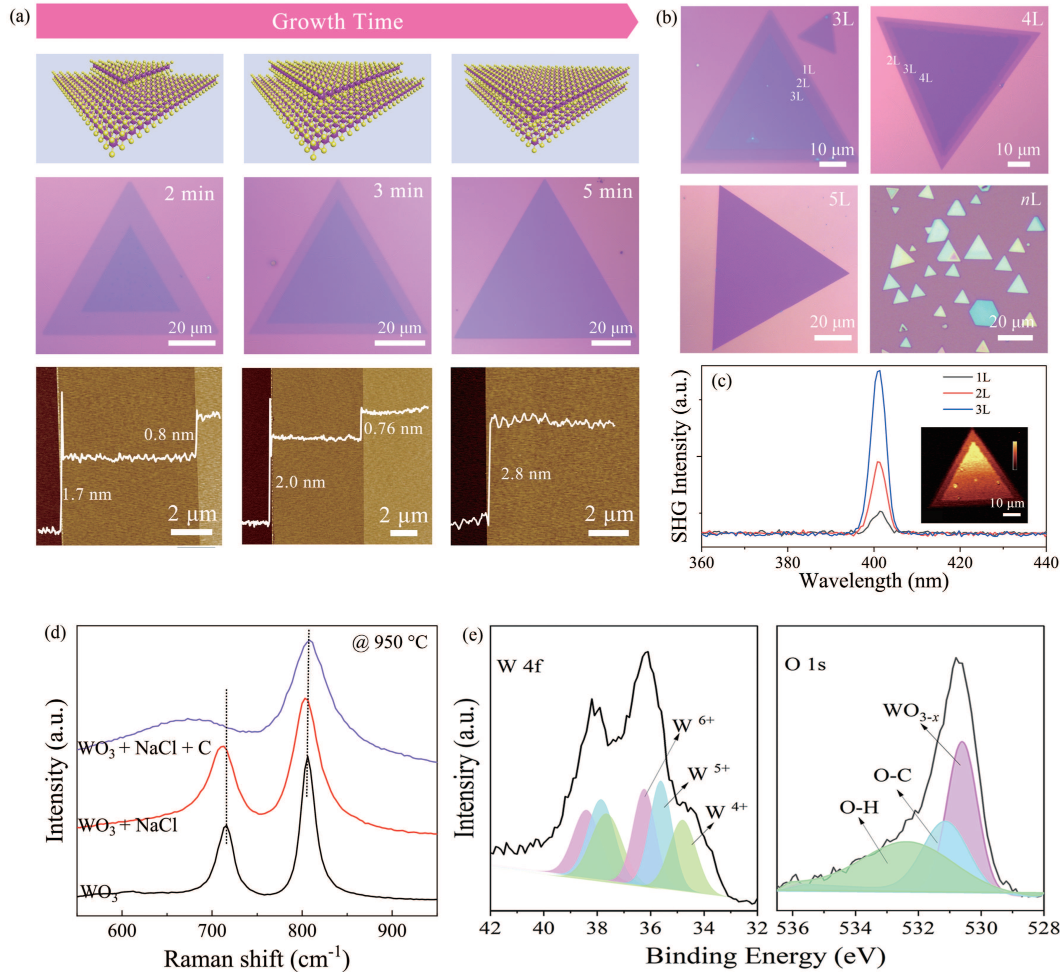

Figure 2 (Color online) Morphology evolution of WS_2 flakes with growth time. (a) Schematic atomic structures, optical images, and local AFM images of the evolution of as-grown bilayer WS_2 flakes with growth time. (b) Optical images of trilayer, tetralayer, quintlayer, and multilayer WS_2 flakes with longer growth time. (c) SHG spectra of trilayer WS_2 flake. Inset: corresponding SHG mapping of the trilayer WS_2 flake. (d) Raman spectra of pristine WO_3 precursors; WO_3 and NaCl mixture; and WO_3, NaCl, and C mixture collected at 950°C. (e) High-resolution XPS spectra of W and O.

Figure 2(c) shows the second-harmonic generation (SHG) spectra of the as-grown WS_2. A single peak can be observed at 400 nm. The gradual increase of the peak intensity with the number of layers confirms the 3R stacked nature [23]. The homogeneity of the corresponding SHG intensity map in Figure 2(c) indicates the uniformity and high crystal quality of the WS_2 atomic layers.

Carbon can play a crucial role as a reductant by reducing the WO_3 precursor to form intermediate WO_{3-x} products with low W valence states. The evolution of the precursor during the heating process was studied and it was verified that carbon exerted a reducing effect on WO_3, in which W has a valence state of 6^+, by converting it to WO_{3-x} with a lower W valence state, as shown in Figure S2. To further investigate the reduction effect of carbon on the WO_3 precursor at high temperatures, a precursor mixture with carbon and another without were separately subjected to the heating process at 950°C. Figure 2(d) shows the Raman spectra of the products. Two Raman peaks at 714.7 and 806.8 cm^{-1} are present in the original WO_3, which are assigned to longer and shorter W-O-W bond stretching modes, respectively [24]. Because the chemical bonds of W^{6+} are stronger than those of reduced tungsten ions (i.e., W^{5+} and W^{4+}), the Raman peaks of the W^{6+} bonds appear at higher energies, whereas those of the W^{5+} and W^{4+} bonds appear at lower energies [25]. For the precursor without carbon, the longer W-O-W stretching mode appears at 712.5 cm^{-1} in the Raman spectrum. In contrast, in the presence of carbon, the Raman peak is dramatically shifted to a lower wavenumber of 676.4 cm^{-1}. This significant shift in the Raman peak indicates the strong reduction effect of carbon on WO_3. Furthermore, the carbon-mixed precursor was collected at a temperature of 950°C and analyzed using X-ray photoelectron spectroscopy (XPS) to evaluate its chemical composition and bonding states. The high-resolution W and O core-level spectra are

shown in Figure 2(e). The high-resolution W 4f peak XPS spectrum can be deconvoluted into six distinct peaks. The W $4f^{7/2}$ peak attributed to W^{6+} is centered at 38.1 eV, while the W^{5+} and W^{4+} peaks appear at the lower energies of 36.6 and 35.5 eV, respectively [26]. This coexistence of reduced tungsten ions (i.e., W^{5+} and W^{4+}) also confirms the reduction effect of carbon. The three components of the core-level O 1s peak were distinguishable by Gaussian fitting. The peak at 530.6 eV can be attributed to lattice oxygen bonded with W while the other two peaks at 531.4 and 532.8 eV correspond to adventitious oxygen bonded with C-O and water, respectively. The characteristic O 1s peak in WO_3 should theoretically appear at 531.0 eV. The observed shift of the O 1s peak by 0.40 eV towards a lower binding energy confirms the presence of an increased number of oxygen vacancies [27]. It can thus be concluded that carbon played a crucial role in the reduction process by effectively reducing WO_3 to WO_{3-x} with a lower W valence state during the heating process. The conversion of WO_3 to WS_2 through sulfurization involves a stepwise transition from W^{6+} to W^{4+}, during which intermediate $WO_{3-x}S_x$ species and WS_x clusters are formed in the vapor precursor [28]. The high W-O bond energy in WO_3 (672 kJ/mol) [29] and differences between the W atom sites of the monoclinic WO_3 cell and WS_2 hexagonal cell (the nearest W-W interatomic distance along the c-axis changes from 0.38 nm in WO_3 to 0.62 nm in WS_2) [30] hinder direct sulfurization by S. The introduction of carbon can help reduce W^{6+} to a lower-valence state, which promotes the sulfurization conversion process. Previous calculations [31] have indicated that the sulfurization of pure WO_3 has a formation energy of 3.44 eV, whereas the formation energy for the sulfurization of WO_{3-x} with oxygen vacancy sites is significantly lowered to 2.55 eV. This difference in formation energies suggests that the sulfurization of WO_{3-x} with oxygen vacancies is more energetically favorable than that of pure WO_3. The introduced carbon increased the likelihood of producing high-density WO_{3-x} intermediates that readily sulfurized to form WS_x clusters in a single step. Hence, our main focus was on the influence of WS_x clusters on the growth process rather than on the multistep sulfurization process from WO_3 to WS_xO_y and from WS_xO_y to WS_x. Previous studies have highlighted the crucial role of WS_x clusters ($x = 1, 2, 3$) in controlling the formation of lateral or vertical crystals on the bottom WS_2 surface. The high W/S ratio atmosphere facilitated by carbon allows different WS_x (WS_3, WS_2, and WS_1) clusters to coexist during the growth process [32]. Previous calculations have also shown that the binding energies of WS_3, WS_2, and WS_1 on the top surface are -3.7, -5.5, and -6.8 eV, respectively, while those at the WS_2 edge are -5.1, -6.7, and -6.4, respectively [33]. Notably, the lowest binding energy of WS_1 on the top surface promotes nucleation and vertical stacking. The WS_1 clusters on the WS_2 crystal surface are also crucial for vertical stacking growth at high W/S ratios because of their large diffusion barrier (4 eV) [33]. Additionally, oxycarbide byproducts such as CO and CO_2 are more likely to be absorbed on the surface of the as-grown WS_2 sheets during the growth process. Adsorption analysis indicates that CO and CO_2 are preferentially absorbed on the top of the hollows and W atoms of WS_2 with the absorption energies of -0.172 and -0.245 eV, respectively. The corresponding adsorption distances are comparable to the van der Waals gap (approximately 3–3.5 Å) between chalcogen atoms. Figure S3 shows the stable absorption positions of CO and CO_2 molecules on the top surface of the WS_2 monolayer. It is likely that the stable absorbed oxycarbide molecules had low mobility on the WS_2 surface and combined with WO_{3-x} intermediates to form W-O-C nucleation sites, which promoted growth along the z-direction. This is consistent with previous findings that bilayer WS_2 growth may be influenced by W-O-C heterogeneous nucleation sites [21]. The precise and highly controlled growth of bilayer WS_2 crystals can ultimately be attributed to the high W/S ratios facilitated by carbon and the presence of heterogeneous nucleation sites generated by the byproduct gas.

The crystalline structure of the obtained bilayer WS_2 crystals was investigated further. The bilayer WS_2 crystals were transferred to a copper grid using the wet transfer method. The corresponding low-magnification SEM image is shown in Figure S4. High-resolution high-angle annular dark-field-scanning transmission electron microscopy (HAADF-STEM) was performed to visually check for the presence of atomic defects. A perfect hexagonal honeycomb shape with no evident vacancy defects was observed (Figure 3(a)). Figure 3(b) shows line plot profiles corresponding to the three rectangular boxes shown from left to right in Figure 3(a). The three distinct contrast intensities that can be clearly identified indicate that the obtained bilayer WS_2 is 3R stacked, which is consistent with previous reports. In 3R stacking, the lattices have a staggered ABC arrangement in which the S atoms of the top layer are aligned with the W atoms of the bottom layer, and both the W atoms of the top layer and S atoms of the bottom layer reside in the hollow [34], as shown in the inset of Figure 3(a). The regularity of the intensity changes in the three different contrast intensities corresponding to columns of W and 2S, W, and 2S atoms indicates the absence of evident S vacancies.

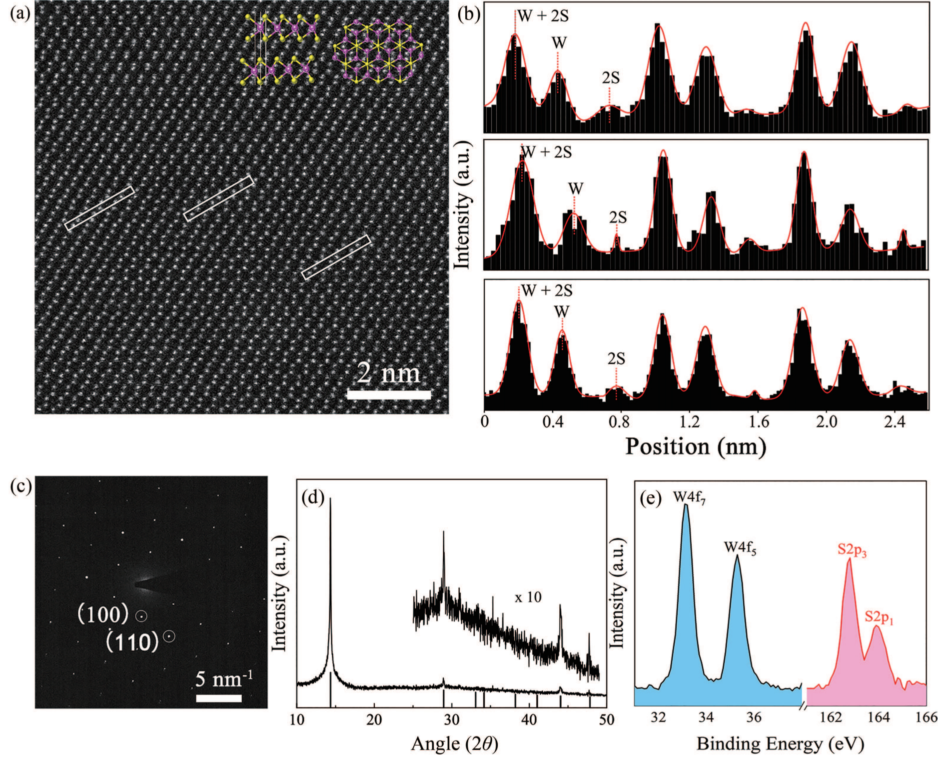

Figure 3 (Color online) Characterization of bilayer WS_2 crystals. (a) HAADF-STEM image of bilayer WS_2. (b) Intensity line profile measured from the labeled regions in (a). (c) SAED pattern of bilayer WS_2. (d) XRD pattern of bilayer WS_2. The peak at 44° belongs to WS_2 with 3R stacking. (e) XPS spectrum of bilayer WS_2.

The selected-area electron diffraction (SAED) pattern shown in Figure 3(c) clearly exhibits one set of hexagonal diffraction spots, which confirms the single-crystal structure of the sample. Furthermore, X-ray diffraction (XRD) was performed to further confirm the stacking structure of the as-grown bilayer WS_2. Figure 3(d) shows the XRD characteristics of the obtained WS_2, which align well with the structure of 3R-stacking WS_2 (JCPDS Card No. 84-1399) and show a highly consistent peak at 44°, which serves as a fingerprint to distinguish it from 2H WS_2. To exclude W-C bonds in the lattice, XPS was performed to determine the chemical composition of the grown bilayer WS_2 sheets. As shown in Figure 3(e), there are prominent peaks at 33.14 and 35.28 eV, which belong to the W^{4+} $f^{7/2}$ and $f^{5/2}$ W core levels, respectively, while the peaks located at 163.75 and 163.93 eV are attributed to S $2p^{3/2}$ and S $2p^{1/2}$ S core levels [35]. The absence of other peaks corresponding to carbon indicates that the obtained bilayer is of high purity.

Field effect transistors (FETs) were fabricated to thoroughly assess the electrical performance of the as-grown bilayer WS_2. The device performance of the FETs was evaluated by applying a gate voltage to both silicon and graphene [36]. The corresponding device diagram and optical image are shown in Figures 4(a) and (b), respectively. More detailed information on the fabrication process is provided in Section 4. Figures 4(c) and (d) show representative transfer ($I_{\rm DS}$-$V_{\rm BG}$) and output ($I_{\rm DS}$-$V_{\rm DS}$) characteristics across the E1-E2 electrodes, respectively. The transfer characteristics exhibited a typical n-type behavior in which the drain current increased as $V_{\rm BG}$ was increased from −60 to 60 V. The maximum ON-state current reached 187 μA under a back gate voltage of 60 V and drain voltage of 2 V. The linear and symmetrical relationships in the output characteristics of the bilayer WS_2 device indicate good ohmic contact between the bilayer WS_2 and metal electrodes. Moreover, utilizing graphene as the backgate and hBN as the gate dielectric (E2-E3 electrodes) allowed the subthreshold characteristics of the transistor to be optimized. As shown in Figure 4(e), the bilayer WS_2 FET exhibited outstanding field modulation in which the change in the channel current exceeded 10^8 times at an ON-state current of 132 μA $V_{\rm Gra}$ = 6 V, $V_{\rm DS}$ = 2 V, $V_{\rm Si}$ = 60 V).

$$\mu = \frac{\mathrm{d}I_{\rm DS}}{\mathrm{d}V_{\rm BG}} \times \frac{L}{W} \times \frac{1}{C \times V_{\rm DS}}, \tag{1}$$

$$\mathrm{SS} = \left[\frac{\mathrm{d}\log_{(I_{\rm DS})}}{\mathrm{d}V_{\rm BG}}\right]. \tag{2}$$

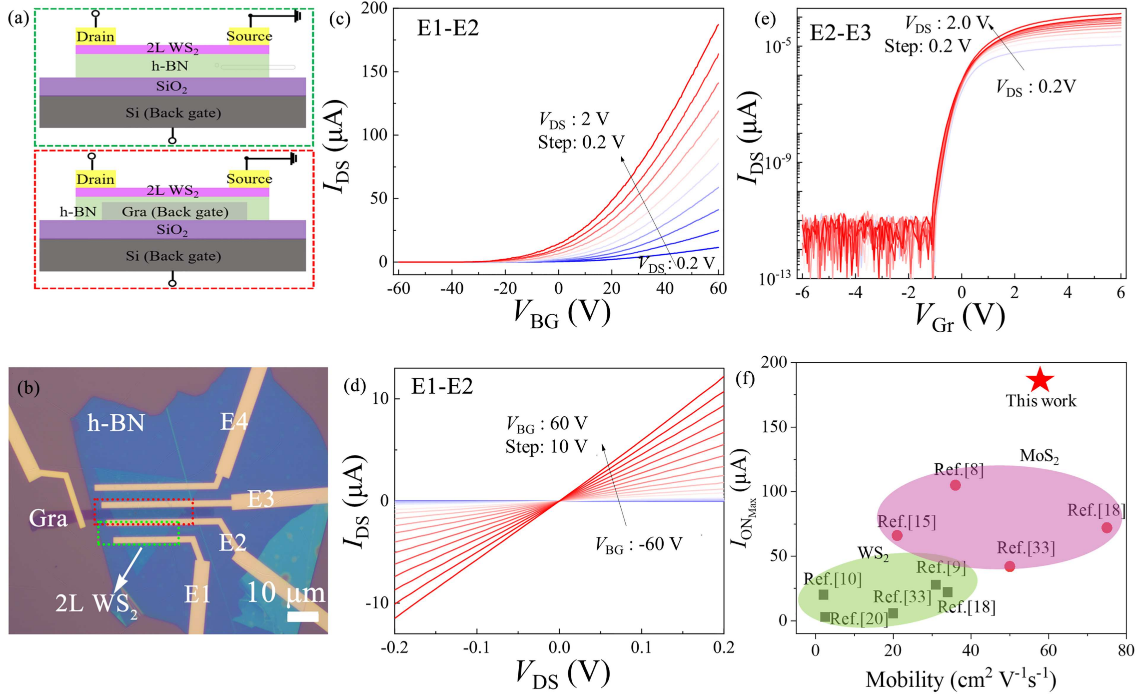

Figure 4 (Color online) Transport properties of bilayer WS_2 FET. (a) Schematic illustration of device structure. (b) Optical image of assembled bilayer WS_2-based FET device. (c) Transfer characteristics and (d) output curves of bilayer WS_2 FET with silicon as backgate. (e) Transfer characteristics of bilayer WS_2 FET with graphene as backgate. (f) Comparison of mobility and on-state current of our bilayer WS_2 FET with those of reported structures.

The mobility and SS were evaluated using (1) and (2). Here, $\frac{L}{W}$ is the ratio of the channel length to width and C is the capacitance of the gate dielectric. $V_{\rm DS}$ and $V_{\rm BG}$ represent the bias voltages applied to the back-gate and drain electrodes, respectively. $I_{\rm DS}$ is the current flowing across the channel. A mobility of 58 $\rm cm^2{\cdot}V^{-1}{\cdot}s^{-1}$ and SS of 148 mV/decade were extracted from Figures 4(c) and (e), respectively. To further assess the performance of our bilayer WS_2 FET, we compare their mobility and on-state current with those reported in the existing literature. As shown in Figure 4(f), the mobility of our bilayer WS_2 FET is superior to those of previously reported WS_2 FETs and comparable to those of bilayer MoS_2 FETs. The mobilities, on/off ratios, measurement conditions, and device structures for all the devices in Figure 4(f) are summarized in Table S1. Moreover, the best on-state current performance amongst the currently reported devices is achieved in our work.

3 Conclusion

In conclusion, we developed a C-assisted chemical vapor epitaxy technique that enables the controlled synthesis of high-quality WS_2 bilayer crystals with high yield, uniform surfaces, and excellent controllability. Our results show that carbon plays a crucial role in reducing oxygen in the WO_3 precursor by enabling the formation of low-valence W intermediates with favorable sulfuration properties. The structural characterization results indicate that the obtained samples have high crystal quality. Transistors were also constructed based on the bilayer WS_2. The achieved mobility, subthreshold swing, and on-state current are among the best reported results. Our work provides an effective and promising strategy for precise layer control during WS_2 growth and offers valuable insights into the potential applications of bilayer TMDs in future electronic devices.

4 Experimental section

Material synthesis. Bilayer WS_2 flakes were synthesized in a quartz tube furnace using an additive-modified CVD technique. First, a mixture of WO_3 (35 mg, 99.9%, Alfa Aesar), NaCl (1 mg, 99.9%, Alfa Aesar), and C (3.5 mg, 99.5%, Aladdin) powder was milled fully and dispersed in a ceramic boat, which

was placed in the center of the furnace. A SiO_2/Si wafer (silicon substrate coating with 300 nm thick oxide) was used as the growth substrate and placed on top of the mixed powder with the polished face down. S powder (350 mg, 99.5%, Sigma-Aldrich) was loaded in the upstream zone of the furnace. C and NaCl were used as additives, and WO_3 and S were used as precursors to grow WS_2. Before heating, the tube furnace was flushed with Ar (1000 sccm) for 5 min to remove residual oxygen. The furnace was then heated to the growth temperature of 950°C at a ramp rate of 26°C$\cdot$min^{-1}. Throughout the process, Ar was used as the carrier gas and a continuous flow rate of 100 sccm was maintained under ambient pressure. The growth process lasted for 5 min and was followed by natural cooling to room temperature. Monolayer WS_2 samples were synthesized through similar steps but without the introduction of carbon powder.

Characterization. The morphology and structure of the WS_2 flakes were characterized using a microscope (Zeiss Axio Scope A1), AFM (Bruker Dimension Icon), and TEM (FEI Themis Z (3.2)). Raman and PL spectra were measured using a confocal microscope system (WITec, Alpha 300R) at an excitation wavelength of 488 nm. The electrical performance of the as-fabricated devices was evaluated using a Lake Shore Probe Station combined with an Agilent B1500A semiconductor analyzer under vacuum conditions at room temperature.

Device fabrication and electrical measurements. Bilayer WS_2 flakes were peeled from the growth substrate to polydimethylsiloxane (PDMS) films using a dry-transfer technique. Few-layer graphene was directly fabricated on a highly p-doped 300 nm SiO_2/Si substrate using the mechanical exfoliation method. Simultaneously, h-BN sheets were directly exfoliated onto the PDMS films. h-BN and bilayer WS_2 were then aligned and transferred onto the graphene flakes layer-by-layer using a transfer stage under an optical microscope to form the WS_2/h-BN/graphene heterostructure. Finally, e-beam lithography (EBL, Raith 150 Two) and metal thermal evaporation were employed to define the electrode patterns and deposit Cr/Au metal (10 nm/50 nm) on the obtained structures. The FETs were fabricated using a lift-off process.

Acknowledgements This work was supported by National Key R&D Program of China (Grant Nos. 2022YFA1402501, 2022YFA-1204300), National Natural Science Foundation of China (Grant Nos. 52372146, 62375081, U22A20138, 51972105, 52221001 62090035), Key Program of Science and Technology Department of Hunan Province (Grant Nos. 2019XK2001 2020XK2001), Science and Technology Innovation Program of Hunan Province (Grant No. 2021RC3061), and Natural Science Foundation of Hunan Province (Grant No. 2021JJ20016), Natural Science Foundation of Tianjin (Grant No. 20JCYBJC00390), and Open Project Program of Key Laboratory of Nanodevices and Applications, Suzhou Institute of Nano-Tech and Nano-Bionics, Chinese Academy of Sciences (Grant No. 22ZS01).

Supporting information Appendix A. The supporting information is available online at info.scichina.com and link.springer.com. The supporting materials are published as submitted, without typesetting or editing. The responsibility for scientific accuracy and content remains entirely with the authors.

References

1 Wang S, Liu X, Xu M, et al. Two-dimensional devices and integration towards the silicon lines. Nat Mater, 2022, 21: 1225–1239
2 Liu Y, Duan X, Shin H J, et al. Promises and prospects of two-dimensional transistors. Nature, 2021, 591: 43–53
3 Sun X, Zhu C, Yi J, et al. Reconfigurable logic-in-memory architectures based on a two-dimensional van der Waals heterostructure device. Nat Electron, 2022, 5: 752–760
4 Li D, Chen M, Sun Z, et al. Two-dimensional non-volatile programmable p-n junctions. Nat Nanotech, 2017, 12: 901–906
5 Ning H K, Yu Z H, Li T T, et al. From lab to fab: path forward for 2D material electronics. Sci China Inf Sci, 2023, 66: 160411
6 Lin Y C, Torsi R, Younas R, et al. Recent advances in 2D material theory, synthesis, properties, and applications. ACS Nano, 2023, 17: 9694–9747
7 Liang J, Zhu X, Chen M, et al. Controlled growth of two-dimensional heterostructures: in-plane epitaxy or vertical stack. Acc Mater Res, 2022, 3: 999–1010
8 Gao Q, Zhang Z, Xu X, et al. Scalable high performance radio frequency electronics based on large domain bilayer MoS_2. Nat Commun, 2018, 9: 4778
9 Shi X, Li X, Guo Q, et al. Ultrashort channel chemical vapor deposited bilayer WS_2 field-effect transistors. Appl Phys Rev, 2023, 10: 011405
10 Yang R, Feng S, Xiang J, et al. Ultrahigh-gain and fast photodetectors built on atomically thin bilayer tungsten disulfide grown by chemical vapor deposition. ACS Appl Mater Interfaces, 2017, 9: 42001–42010
11 Liu X J, Yu Y, Liu D, et al. Coupling of photon emitters in monolayer WS_2 with a photonic waveguide based on bound states in the continuum. Nano Lett, 2023, 23: 3209–3216
12 Liu Y, Guo J, Zhu E, et al. Approaching the Schottky-Mott limit in van der Waals metal-semiconductor junctions. Nature, 2018, 557: 696–700
13 Zhang Z, Liu Y, Dai C, et al. Highly selective synthesis of monolayer or bilayer WSe_2 single crystals by pre-annealing the solid precursor. Chem Mater, 2021, 33: 1307–1313
14 Moon G, Min S Y, Han C, et al. Atomically thin synapse networks on van der Waals photo-memtransistors. Adv Mater, 2023, 35:

15 Fang M, Wang F, Han Y, et al. Controlled growth of bilayer-MoS_2 films and MoS_2-based field-effect transistor (FET) performance optimization. Adv Elect Mater, 2018, 4: 1700524
16 Zhou J, Lin J, Huang X, et al. A library of atomically thin metal chalcogenides. Nature, 2018, 556: 355–359
17 Liu L, Li T, Ma L, et al. Uniform nucleation and epitaxy of bilayer molybdenum disulfide on sapphire. Nature, 2022, 605: 69–75
18 Zhang X, Nan H, Xiao S, et al. Transition metal dichalcogenides bilayer single crystals by reverse-flow chemical vapor epitaxy. Nat Commun, 2019, 10: 598
19 Wang Q, Tang J, Li X, et al. Layer-by-layer epitaxy of multi-layer MoS_2 wafers. Natl Sci Rev, 2022, 9: nwac077
20 Huang L Y, Li M Y, Liew S L, et al. Area-selective growth of two-dimensional mono- and bilayer WS_2 for field effect transistors. ACS Mater Lett, 2023, 5: 1760–1766
21 Liang J, Zhang L, Li X, et al. Carbon-nanoparticle-assisted growth of high quality bilayer WS_2 by atmospheric pressure chemical vapor deposition. Nano Res, 2019, 12: 2802–2807
22 Xue H, Wu G, Zhao B, et al. High-temperature in situ investigation of chemical vapor deposition to reveal growth mechanisms of monolayer molybdenum disulfide. ACS Appl Electron Mater, 2020, 2: 1925–1933
23 Zeng Z, Sun X, Zhang D, et al. Controlled vapor growth and nonlinear optical applications of large-area 3R phase WS_2 and WSe_2 atomic layers. Adv Funct Mater, 2019, 29: 1806874
24 Frey G L, Rothschild A, Sloan J, et al. Investigations of nonstoichiometric tungsten oxide nanoparticles. J Solid State Chem, 2001, 162: 300–314
25 Qian J, Zhao Z, Shen Z, et al. Oxide vacancies enhanced visible active photocatalytic $W_{19}O_{55}$ NMRs via strong adsorption. RSC Adv, 2016, 6: 8061–8069
26 Li X, Zhang J, Zhou N, et al. Insight into the Role of H_2 in WS_2 growth by chemical vapor deposition. ACS Appl Electron Mater, 2021, 3: 5138–5146
27 Imran M, Alenezy E, Sabri Y, et al. Enhanced amperometric acetone sensing using electrospun non-stoichiometric WO_{3-x} nanofibers. J Mater Chem C, 2021, 9: 671–678
28 Lan C, Li C, Ho J C, et al. 2D WS_2: from vapor phase synthesis to device applications. Adv Elect Mater, 2021, 7: 2000688
29 van der Vlies A J, Kishan G, Niemantsverdriet J W, et al. Basic reaction steps in the sulfidation of crystalline tungsten oxides. J Phys Chem B, 2002, 106: 3449–3457
30 Liu Z, Murphy A W A, Kuppe C, et al. WS_2 nanotubes, 2D nanomeshes, and 2D in-plane films through one single chemical vapor deposition route. ACS Nano, 2019, 13: 3896–3909
31 Miakota D I, Unocic R R, Bertoldo F, et al. A facile strategy for the growth of high-quality tungsten disulfide crystals mediated by oxygen-deficient oxide precursors. Nanoscale, 2022, 14: 9485–9497
32 Li F, Feng Y, Li Z, et al. Rational kinetics control toward universal growth of 2D vertically stacked heterostructures. Adv Mater, 2019, 31: e1901351
33 Pan B, Zhang K, Ding C, et al. Universal precise growth of 2D transition-metal dichalcogenides in vertical direction. ACS Appl Mater Interfaces, 2020, 12: 35337–35344
34 Chen J, Jung G S, Ryu G H, et al. Atomically sharp dual grain boundaries in 2D WS_2 bilayers. Small, 2019, 15: e1902590
35 Chen Y, Jiang Y, Yi C, et al. Efficient control of emission and carrier polarity in WS_2 monolayer by indium doping. Sci China Mater, 2021, 64: 1449–1456
36 Sun X X, Zhu C G, Liu H W, et al. Contact and injection engineering for low SS reconfigurable FETs and high gain complementary inverters. Sci Bull, 2020, 65: 2007–2013